ACS APPLIED NANO MATERIALS

Optoporation and Recovery of Living Cells under Au Nanoparticle Layer-Mediated NIR-Laser Irradiation

Timofey E. Pylaev,* Yuri Efremov, Elena S. Avdeeva, Artem A. Antoshin, Anastasiia I. Shpichka, Tatiana M. Khlebnikova, Peter Timashev, and Nikolai G. Khlebtsov

Cite This: https://doi.org/10.1021/acsanm.1c02734

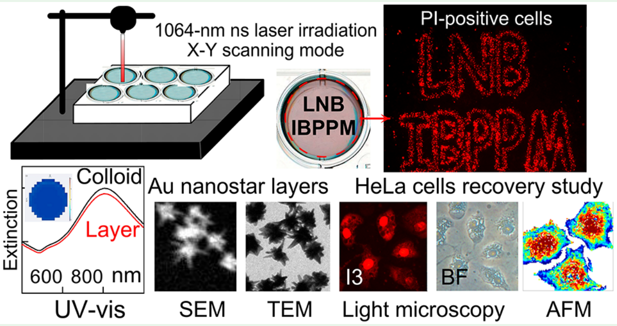

ABSTRACT: Laser optoporation systems are now increasingly used for intracellular delivery. However, data on the response of cells to radiation-induced nondamaging changes in the integrity of the membrane lipid bilayer remain limited. Traditionally, confocal laser scanning microscopy and electron microscopy are used for such studies, but they have limitations for in situ experiments. The modern capabilities of atomic force microscopy (AFM) combine the resolution of electron microscopy and the possibility of noninvasive lifetime imaging of cells in vitro. Herein we used long-term AFM mapping integrated with fluorescence microscopy imaging for investigation of the whole cell cycle from irradiation time point to the total recovery to the intact cell state. For the first time we performed a comprehensive study of long-term posteffects of continuous laser and pulsed laser on the mechanical properties and the membrane recovery of HeLa cells grown on the Au nanoparticle layers of various morphologies. The set of nonpenetrating agents with various sizes ranging from 1 to 1.5 nm for propidium iodide (PI) up to 6−8 nm for 40 kDa FITC-labeled dextran was used to control the delivery efficacy. The main parameters recorded with AFM scanning of cells are Young's modulus (YM) and the cell surface topography. We revealed that self-healing of HeLa cell from the moment of irradiation to complete restoration of the membrane integrity is lasting 22−30 h when using a continuous-wave source and 2−5 h when using a pulsed laser, respectively. The estimated time elapse was in good correspondence with the relative change in YM during the entire experiment. Our findings demonstrate the capability of AFM coupled with fluorescent microscopy for further in situ investigations of the morphological and functional state of the cells exposed to the influence of other external conditions.

KEYWORDS: *Au nanostars, nanoparticle layers, HeLa cells, plasmid DNA, laser transfection, optoporation, atomic-force microscopy, cell mechanical properties*

1. INTRODUCTION

The intracellular delivery of nucleic acids and proteins, termed as transfection, is a crucial step in the development of genetically engineered cells.[1] Correction of defective organ functions, treatment of diseases, or modeling of physiological and pathological behaviors can be realized by means of cell-based therapies. During the last three decades a broad list of viral[2] and nonviral[3] systems, based on the use of chemical agents,[4] nanomaterials,[5] and physical forces have been developed. However, the existing drawbacks related to low efficacy, poor cell viability, limited scalability, multiple-type cells, and cargoes incompatibility still remain topical issues.

One of the most promising and intensively studied delivery strategies nowadays is based on micro- and nanoparticles (NPs), which encapsulate or adsorb DNA molecules,[6] thus improving their penetration ability and prevention from endonucleases.[7] Among all types of nanomaterials used as delivery platforms[8−10] one of the most favorable are AuNP.[11] The advantages of AuNP arise from their unique physicochemical properties,[12] such as low cytotoxicity[13] and immunogenicity,[14] availability of protocols for reproducible and scalable chemical synthesis,[15] and surface modification and functionalization with biospecific ligands.[16]

Another delivery strategy is based on the use of physical forces to enhance the cell membrane permeability. The physical systems such as microinjection, electroporation, and sonoporation are well-known and widespread in laboratory applications. Alternatively, the laser optoporation (also known as laser transfection or optoinjection) has received much attention during the past decade.[17] The optoporation systems can be classified by the laser source parameters (wavelength,

Received: September 2, 2021
Accepted: November 9, 2021

Scheme 1. Representative Scheme of Plasmonic Optoporation Experimental Setup[a]

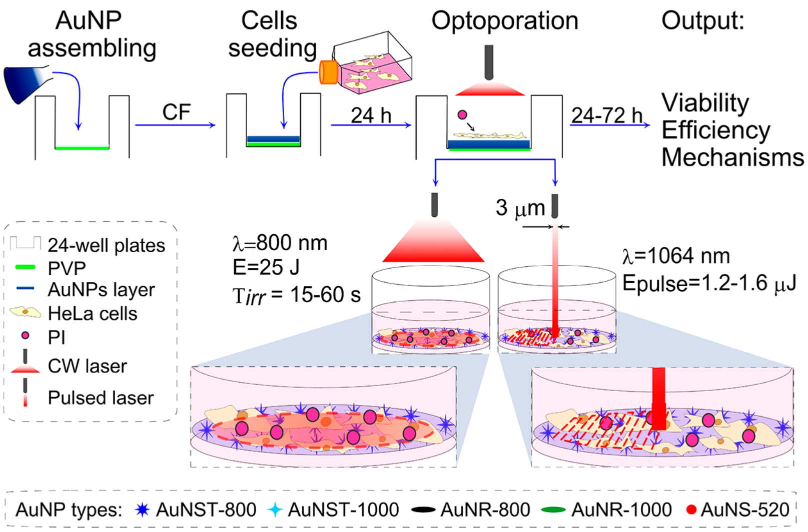

[a] The icons depicting AuNP types, pulsed and CW lasers are used in all subsequent figures of this study.

pulse frequency, incident energy, beam thickness, etc.) or by the type of the mediators that enhance laser energy if any are used. Among the broad list of nanomaterials used as heat transducers in optoporation systems, AuNPs can be considered as one of the most effective due to their strong wavelength-dependent plasmonic properties. The principle of the plasmonic-assisted optoporation is as follows. The NIR irradiation of randomly adsorbed AuNPs initiate the local heat generation that evokes the cavitation microbubbles formation thus leading to the increased membrane permeability for nonpenetrating agents.[18] Despite the estimated worth efficiency and simplicity of this approach, the main disadvantage is addressed to the nonspecific and uncontrolled adsorption of NPs on the membrane with possible penetration into the cytosol that can reduce the cell viability. One of the ways to overcome the limitations is to use plasmonic substrates instead of incubating the cells with colloidal NPs. Such platforms serve both as cell culture substrates and surfaces close to the cells for optoporation.[19−22] Thus, the ineligible incubation step is reduced, and the unexpected side-effects arising from the interactions between NPs and cells that affect viability are minimized. Recently, we proposed a simple universal centrifuge (CF) based approach for AuNP assembling directly on the culture plastic.[23] Highly efficient (about 97%) and safe optotransfection of HeLa cells with plasmid DNA[24] was provided on the platforms of Au nanostars layers[25] using an 808 nm continuous-wave (CW) laser. However, the main disadvantage of CW irradiation is bulk heating of the cell medium that has a sufficient negative effect both on cargoes and cells.[26] In contrast, the optoinjection of cells with a pulsed laser is considered to be safer and more high-throughput.[19,27,28] The main advantages of a pulsed laser are extremely short pulse duration (nano- or femtoseconds) at a relatively low energy, the ability for point-by-point adjustment of individual parameters of the light beam, and the possibility of the 2-D and 3-D scanning irradiation modes for better performance.

Here we report a mechanistic study of the HeLa cells response after optoporation on the AuNP monolayers using CW and pulsed NIR irradiation. Specifically, we investigated the effects of the NP geometry, spectral characteristics, and the irradiation modes of 808 nm CW laser and 1064 nm ns pulsed laser by a model set of optoporation experiments on the delivery of nonpenetrating dyes with various sizes ranging from 1 to 1.5 nm for PI up to 6−8 nm for 40 kDa FITC-labeled dextrane to HeLa cells. For this purpose, we fabricated Au nanostars and Au nanorods layers with plasmon resonance (PR) bands located at 800 and 1000 nm, respectively, directly on the bottoms of culture plastic (24-, 96- wells plate or 35 mm Petri dishes format). The layers of AuNP spheres with a PR band 520 nm located distantly from the wavelengths of the used lasers sources served as a negative control. To examine the HeLa cells response after optoporation on the plasmonic platforms, we used the lifetime AFM scanning combined with standard live/dead fluorescence microscopy bioimaging and respiratory assays for cell viability. The time-dependent mechanical parameters recorded by AFM were cells surface topography and the YM. The duration between the moment of irradiation to complete restoration of the cell membrane integrity was about 22−30 h (when using a CW laser) and 2−5 h (for a pulsed laser) depending on the cargo molecule size and correlated well with the relative change in YM during the entire experiment. To the best of our knowledge, the presented combined AFM-based approach has not been reported previously, and it is a convenient and informative tool for in situ investigations of the behavior of living cells after optoporation on plasmonic platforms.

2. MATERIAL AND METHODS

2.1. Preparation and Characterization of NP Layers. The AuNP layers were obtained by our recently developed approach[14] on the well bottoms of the polystyrene culture 24- and 96-well plates or Petri dishes with 35 mm diameter (Corning Costar, GEB). The synthetic procedures for obtaining the AuNP colloids are given in section S2 (Supporting Information). Briefly, the well bottoms were treated with 1% ethanol solution of PVP by incubation for 1 h at room temperature. The appropriate volume of the PVP solution was adjusted to the corresponding well area to completely cover the bottom. Then the wells were washed several times with ethanol and Milli-Q water, followed by the addition of as-prepared NP colloids (AuNST-800, AuNS-520) or pegylated NPs (AuNST-1000, AuNR-800 and AuNR-1000) with the particle concentration adjusted to the desired Au surface densities. Then the plates were centrifuged using

Eppendorf 5810R equipped with a bucket rotor for plates. The CF regimes were individually chosen for each AuNP type to obtain total sedimentation of the particles. Finally, the supernatant was discarded, the wells were washed thrice with distilled water, dried in air, and stored at 4 °C for later use. Prior to the cell cultivation, the plates with AuNP layers were sterilized in 96% ethanol for 30 min, followed by UV treatment for 15 min.

The extinction spectra of AuNP layers and the supernatants after CF were measured on a Tecan Spark 10 M plate spectrophotometer. Coating uniformity was assessed by measuring the absorbance of the wells in 2-D scanning mode at a fixed wavelength fitted to the corresponding PR for each sample. Additionally, the AuNP layers were prepared for SEM imaging on the special substrates (wafers) similar to the above procedure. Briefly, the silicon wafers 1 × 1 cm in size were cleaned with Piranha solution (a mixture of pure sulfuric acid and hydrogen peroxide in a ratio of 4:1, respectively) and washed with water. Then they were placed in the wells of 12-well plates, treated with PVP solution and CF after addition of the AuNP colloids, washed, and dried. Then the samples were visualized without additional deposition at a voltage of 30 kV. The AuNP layers topography was visualized on the samples prepared on the 35 mm Petri using high-resolution AFM microscopy. The imaging was performed in air with AFM BioScope Resolve (Bruker, Santa Barbara, CA) using Peak-Force Tapping mode with ScanAsyst-Air cantilevers (Bruker) with a nominal tip radius of 2 nm. At least 30 images were processed with more than 1000 particles for each sample of the assembled AuNPs.

2.2. Optoporation of the Cells Grown on the AuNP Layers.

HeLa cell lines were cultured in DMEM/F-12 (Dulbecco's Modified Eagle Medium/Nutrient Mixture F-12) medium containing 1× GlutaMax, 15 mM HEPES, 10% FBS, and 1% antibiotic/antimycotic solution (all ThermoFisher Scientific) in a humidified 5% CO_2 atmosphere at 37 °C. Prior the experiments, the cells were seeded on the Petri dishes (for AFM measurements) or well plates (for optoporation only) with AuNPs layers and grown to an ~70% confluent monolayer. Then the medium was refreshed to the serum-free DMEM containing 15 μM PI, and the cells were subjected to a single CW or pulsed laser irradiation (Scheme 1).

We used a CW laser with 8 W power and 808 nm wavelength (Optronics, Russia) with following parameters set: incident intensity 1 W/cm^2, the single irradiation area about 15 × 15 mm, the defocused beam with a nonuniform intensity over the entire area, exposure time adjusted to the AuNP type, and particle surface density in the range from 15 to 150 s. The nanosecond pulse laser (LSF-20H Mopa, HG-Tech, China) parameters were as follows: wavelength 1064 nm, irradiation power 0.5% of the nominal 20 W, pulse duration 8 ns, pulse energy adjusted to the AuNP type, particle surface density in the range from 1 to 3 μJ, the beam diameter in the waist of 3 μm, the irradiation in a 2-D scanning mode with a linear movement with a 200 μm line offset, and scanning speed of 0.05 m/s. The cells were incubated at 37 °C for 15 min after the laser treatment, followed by single-step washing with 1 × PBS to avoid the uncontrollable penetration of excess PI molecules.

The optoporation efficacy was assessed via fluorescence microscopy imaging as described in section S3 (Supporting Information). The cell viability was checked at all experimental stages; the procedure is given in section S4 (Supporting Information).

2.3. Atomic Force Microscopy of Living HeLa Cells.

All AFM measurements were performed using Bioscope Resolve AFM (Bruker, Santa Barbara, CA) mounted on Axio Observer inverted optical microscope (Carl Zeiss, Germany). The microscope has a heated stage, and the sample temperature was kept constant at 37 °C during the experiments with cells. PeakForce QNM-Live Cell cantilevers were used (PFQNM-LC-A-CAL, Bruker AFM Probes, Camarillo, CA, U.S.A.), short paddle-shaped cantilevers with a precalibrated spring constant (values were in the range of 0.06−0.08 N/m), and a 70 nm radius 17-μm-long tip. The cantilever deflection sensitivity (nm/V) was calibrated from the thermal spectrum directly in the dish with a sample using the precalibrated value of the spring constant.[29,30] The AFM measurements were performed in serum-free DMEM medium with 25 mM HEPES, and the irradiation was performed in the same medium. After and between the AFM measurements, the medium was changed for a complete DMEM medium with a serum to promote cell recovery.

Nanomechanical maps were acquired in the fast force volume mode with a typical map size of 80 × 80 μm and from 32 × 32 to 80 × 80 measurement points. A vertical ramp distance of 3 mm, a vertical piezo speed of 183 mm/s, and a trigger force of 0.5−1 nN were used, which resulted in an indentation depth of 400−900 nm. The force curve processing was done according to our previously developed procedure.[30,31] First, the force curves were corrected for the hydrodynamic drag, and the zero-force level was defined. Then, the apparent elastic YM was calculated by fitting the force curves with the Hertz's model with a bottom-effect correction.[32]

$$F = \frac{4}{3} f_{\mathrm{BEG}}(\delta) \frac{E}{1 - \nu^2} R^{1/2} \delta^{3/2} \tag{1}$$

where F is the measured force, δ is the indentation depth, R is the tip radius, ν is the Poisson's ratio of the sample (was considered to be 0.5 for cells), and $f_{\mathrm{BEG}}(\delta)$ is the bottom-effect correction factor.[32] The resulting AFM maps represent the topography reconstructed from the contact point positions of the curves (z, in μm) and the distribution (map) of YM (Pa, logarithmic scale). From the entire map, force curves were selected that fell on individual cells. YM values were averaged over such curves to obtain a mean value for single cell for subsequent comparison. The summarized data are presented in the form of point box-plot diagrams, where each point corresponds to the mean YM of each cell, the box-plot diagram indicates the median, 25th and 75th percentiles. In figure captions, the data are presented as mean ± standard deviation for a group of cells.

3. RESULTS AND DISCUSSION

3.1. Characterization of NPs.

A partial overlap between the AuNP extinction maximum wavelength and the laser wavelength is crucial for obtaining the highest thermoplasmonic effect of irradiation.[33] Therefore, we adjusted the PR bands of as-prepared AuNPs to the wavelengths of laser sources −808 nm CW laser and 1064 pulse laser (Figure S1A, Supporting Information). The other parameter that may affect the outcome of optoporation is AuNP geometry. We fabricated five types of AuNPs with different geometries and PR bands, specifically star-shaped AuNST-800 and AuNST-1000, rod-shaped AuNR-800 and AuNR-1000 with PR bands at 800 and 1000 nm, respectively, and one type of spherical particle with a PR band near 520 nm (AuNS-520). For brevity, hereinafter in the text, we use the abbreviated name of the colloid with the corresponding average value of PR wavelength. The measured characteristics of all as-prepared AuNPs, namely extinction spectra, representative TEM images, DLS average size, zeta-potential, mass-molar concentration, and particle number concentration are given in section S5 (Supporting Information).

Several points should be mentioned about AuNST-800 in regard to choosing them as the most suitable for plasmonic layers-mediated optoporation. First, the as-prepared AuNST-800 have the PR maximum in the visible region at 760−780 nm and a broadened band with half-width about 60−80 nm and sufficient extinction even in the NIR region at 1100 nm,[34] thus, overlapping with the wavelengths of CW and pulsed lasers both (Figure S1A, Supporting Information). On the other hand, the optimized protocol for AuNST synthesis,[35] is rapid (the synthesis takes about 30 min), well reproducible and scalable. Note that the seed-mediated synthesis of AuNRs with similar PR band near 800 nm[36] takes about 30 h with additional PEGylation step lasting overnight. Third, the

AuNSTs-800 can be potentially self-assembled[15] as a non-equipment alternative to CF but with the reduced quality of resulting layers. In contrast, the self-sedimentation of AuNR-800 is nonavailable due to its small weight compared to that of the AuNSTs-800 (Table S1, Supporting Information).

Finally, we assume that the star-like shape contributes to a local enhancement of the electromagnetic field at the ends of the spines under the influence of laser radiation,[35] which may be one of the mechanisms for increasing the permeability of cell membranes during optoporation.

On the contrary, the as-prepared AuNR particles had a positive zeta potential due to the surface cationic surfactant CTAB. In this regard, the AuNR samples were modified with PEG molecules. Thus, the resulting zeta potential of the AuNR-PEG particles had a negative sign (Table S1, Supporting Information), and the cytotoxic CTAB layer[37] was replaced by the biocompatible polymeric ligand PEG.[34]

3.2. Characteristics of AuNP Layers. The quality control of the obtained AuNP layers is crucial for further experiments on cell optoporation. We hypothesized that the ideal plasmon substrate should be presented by highly ordered single-assembled AuNPs (not aggregated) in order to provide the most uniform sensibilization of laser radiation. Another critical parameter is the interparticle distance, as it is well-established that the optical properties of the assembled plasmonic NPs are dramatically changed by the decrease of the interparticle distance lower than the particle size, known as the plasmonic coupling effect.[38] Thus, in order to investigate the effect of interparticle distance, we obtained the AuNP layers with different packing density. It is notable that the highest values of the coating uniformity and adsorption rate can be obtained by optimizing only the CF modes corresponding to the each AuNP type. The desired layer packing density can be obtained by using the colloid with the appropriate optical density. In the below subsections we provide a detail description of the physicochemical quality control for the obtained AuNP layers as well as the biocompatibility monitoring.

3.2.1. Coating Uniformity. The uniformity of AuNP assemblies was examined using a special 2-D scanning option of the plate reader Tecan Spark 10M. Specifically, the measurements were performed as follows: first, the extinction spectra was recorded for each well to check the PR wavelength, then the extinction was measured on the fixed wavelength in a 2-D scanning mode on the entire well bottom area divided into the box with 3 × 3 μM mesh. The data was processed using a standard Tecan software and output in 2-D monochrome diagrams (Figure 1A–E, insets). The coating uniformity was estimated in terms of color gradient that indicates the fluctuations of the extinction from the averaged value. The differences between the PR wavelengths and the half-widths of the measured spectra of the layers and the initial colloids no more than 5–7% indicated the nonsufficient aggregation during the particle assembling and the preservation of the plasmonic properties. Thus, using the described prompt and simple UV–visible screening with no more than 5 min for measuring and processing data for a 96-well plate, we checked the suitability of the obtained layers for further use and discarded the low-quality samples. The topography of as-prepared layers was visualized by SEM, and the representative images are exemplified in Figure 1F–H. One can see that the AuNR-800 and AuNS-520 layers are presented by individually ordered particles with small aggregates formed of several particles, while AuNST-800 layers contained larger aggregates of sticked stars by spiky ends. Nevertheless, the presence of aggregates with less than micron sizes had no significant effect on the further HeLa cells cultivation and optoporation results (see below the sections discussing the optoporation experiments).

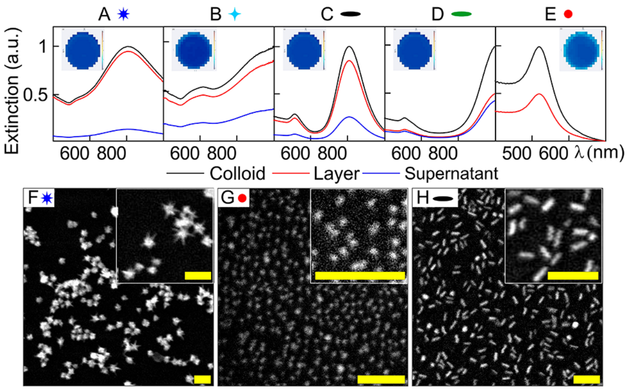

Figure 1. Normalized extinction spectra of initial colloids, supernatants after CF, obtained layers and representative images of the uniformity degree (on the insets) of (A) AuNST-800, (B) AuNST-1000, (C) AuNR-800, (D) AuNR-1000, and (E) AuNS-520 layers. Overview and enlarged (inset) SEM micrographs of (F) AuNST-800, (G) AuNS-520, and (H) AuNR-800 layers. The scale bars are 100 nm.

3.2.2. Adsorption Value. Another important physicochemical parameter of the AuNP layers is the particle adsorption (θ), characterizing the relative particle deposition upon the CF. The total assembling of the particles from the initial colloid was set as 100%. The average θ value for each well with the AuNP layer was estimated as the difference, expressed as a percentage, between the average extinction (estimated at least 3-fold measurements in the UV–visible range) of the original colloid at PR wavelength and the average extinction of the corresponding supernatant obtained after CF in optimized modes. The representative extinction spectra for all types of NPs are exemplified in Figure 1A–E. Using this simple approach, the θ was estimated for the obtained AuNP layers of different particle geometry and packing density, and the resultant adsorption isotherms are represented in Figure 2.

It is notable that the adsorption of AuNST-800 was about 96%, and it was highest among all other studied AuNP types. The θ of AuNR-800 was about 82%, comparable to the θ of

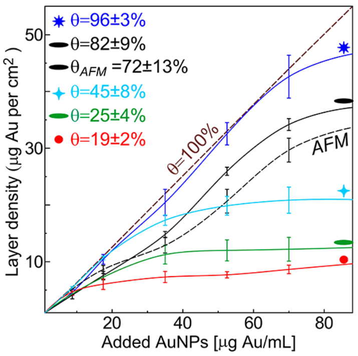

Figure 2. Experimental adsorption isotherms of AuNP layers, calculated from UV–vis data (solid curves) and AFM data (black dashed curve). Theoretical adsorption of a layer with θ = 100% presented as a brown dashed curve.

Table 1. Optimal CF Modes, Average Values of Adsorption (θ), Experimental and Calculated Values of the NPs Packing Density in Terms of Particles Number Per Unit Area (N_L), and Au Mass Per Unit Area (C_L)[a]

	CF modes		UV–vis based data			calculation for θ = 100%	calculation for absolute monolayer	
NP type	RCF (a.u.)	t (min)	θ (%)	C_L (μg/cm^2)	N_L (10^8 part./cm^2)	N_L (10^8 part./cm^2)	C_L (μg/cm^2)	N_L (10^8 part./cm^2)
AuNST-800	1000	5	96 ± 3	37.0 ± 3.6	3.3 ± 0.3	3.5 ± 0.4	327.0 ± 0.4	26.0 ± 1.9
AuNST-1000	1000	5	45 ± 8	20.0 ± 3.5	7.3 ± 0.8	16.0 ± 1.9	44.0 ± 2.1	16.0 ± 2.1
AuNR-800	2000	20	82 ± 9	37 ± 2	1200 ± 156	146 ± 13	114.5 ± 12.0	3800 ± 494
AuNR-1000	1000	10	25 ± 4	11.0 ± 1.6	750 ± 83	3000 ± 278	18.3 ± 1.4	1250 ± 130
AuNS-520	2000	30	19 ± 2	11 ± 2	33.0 ± 2.4	168 ± 15	1666 ± 159	5000 ± 493

[a] All data is exemplified for the layers with C_L = 44 μg/cm^2, and the values are presented as means with standard deviations (n = 20).

AuNST-800, while the θ of other AuNPs was significantly lower, ranging from 19 to 45% (Figure S2, Supporting Information). The relatively low adsorption value of AuNS-520 can be explained by the rather small particle size (15 nm compared to 50−150 nm in the AuNST-800 and AuNR-800), restricting the particle sedimentation upon CF with high adsorption without particle aggregation.

3.2.3. Surface Packing Density. The preparation of AuNP layers with the required 2-D particle packing density (N_L, particle number per square cm) or designated in terms of surface Au content ($C_{\mathrm{L},}$ μg/cm^2) was achieved by using the colloids with appropriate optical densities. The calculations of 2-D Au contents are given in section S6 (Supporting Information).

Let us consider the definition of the working range of the NPs packing densities with regard to further optoporation experiments. The minimum packing density was found from the considerations of significant plasmonic effect resulting in the enhanced permeability of HeLa cells for PI upon laser irradiation with CW or pulsed laser. Specifically, the lower threshold C_L of AuNS-800 was estimated as 4.2 μg/cm^2. The upper threshold C_L of AuNS-800 was estimated as 32.7 μg/cm^2, so that the irradiation of the HeLa cells on this layer even under the slight regimes significantly affected their viability. The detailed description of the optoporation results will be given below in section 3.2.5. Nevertheless, even a high packing density of 50 μg/cm^2 was less than the calculated data for the absolute monolayer of the AuNS-800 assembled with the interparticle distance lower than the particle size. Thus, the obtained plasmonic substrates are formed from rare nanoparticle monolayers with no interparticle effects that influence optoporation. The packing density designated in terms of particle number per unit area (N_L), was calculated from the corresponding C_L value taking into account the volume particle number (N_0) in the as-prepared colloids (Table S1, Supporting Information). The estimated experimental data and the calculated values of the packing density in terms of Au content and the particle number per unit area are summarized in Table 1 for the layers of all used AuNP and exemplified to the C_L = 44 μg/cm^2.

It should be noted that the described UV−vis based approach is indirect and gives only approximate data for packing density and coating uniformity of AuNP layers. The precise quantitative characteristics can be obtained using the methods with in situ visualization performance and nanoscale resolution, such as TEM and AFM imaging. However, the standard TEM with sampling on special metal grids is also limited for direct observation of large-scale samples. To undergo these limitations, we used the lifetime AFM microscopy as the most convenient tool for topographical mapping of AuNP layers directly on the culture plastic. The AFM images and the corresponding extinction spectra of the samples 1, 2, and 3 of the AuNR-800 layers with C_L (UV−vis data) values of 7 ± 0.6, 14 ± 1.3, and 28 ± 3 μg/cm^2 are presented in Figure S2 (Supporting Information) and AuNST-800 layers with C_L (UV−vis data) values of 7 ± 0.4, 14 ± 1.1, and 28 ± 2.7 μg/cm^2 are presented in Figure S3 (Supporting Information), respectively.

As soon as the AFM measurements were carried out directly on the culture plastic instead of the special mica substrates for AFM with low signal-to-noise ratio, the AFM images of AuNST-800 layers (Figure S3, Supporting Information) had insufficient resolution for the quantitative processing due to the spiky morphology and polydispersity of the AuNST-800 particles. On the contrary, the AFM images of the AuNR-800 layers were convenient for further quantitative analysis due to the simple rodlike geometry of the particles. The AFM images processing included the estimation of the following parameters: the particle number per unit area, the interparticle distance and the ratio of aggregated and nonaggregated particles per unit area. The defined values of average particle number per unit area for samples 1, 2, and 3 of the AuNR-800 layers were 2.1 ± 0.3 × 10^{10}, 13 ± 1.2 × 10^{10}, and 40 ± 3.7 × 10^{10} particles/cm^2, respectively (Table S2, Supporting Information). It should be noted that the packing density in terms of the particle number per unit area (N_L), estimated by the processing of AFM images was in good correlation (at the order level) with the correspondent data for the same samples obtained using standard UV−vis based approach.

To summarize the above discussion, we can conclude that we assembled AuNPs with different geometry and desired parameters directly on the culture plastic using a recently developed simple CF-based approach[23] and well-characterized the obtained layers using a UV−vis based approach in parallel with direct AFM-mapping.

3.2.4. Photo- and Chemical Stability and Biocompatibility Tests. We estimated the physicochemical stability and the maintenance of plasmonic properties, as well as the macroscopic mechanical safety of the obtained coverage on the plastic surfaces. Additionally, we estimated the biocompatibility of the AuNP layers and the effects of laser irradiation on the cell viability under experimental conditions. The obtained results are represented in section S7 (Supporting Information).

Next, we performed qRT-PCR analysis of genes expression, associated with stress response and apoptotic processes in HeLa cells. The description of sample preparation and assaying is given in section S8 (Supporting Information). The results of the qRT-PCR assay showed no significant increase in the level of pro-apoptotic genes and antiapoptotic genes expression level in all analyzed experimental samples (optoporated) compared with that of the control. The mean expression levels of antiapoptotic genes decreased by 11.7% (relA), respectively

Table 2. Output Results for HeLa Cells Optoporation upon CW and Pulsed Lasers under Selected Irradiation Modes and Optimized AuNP Layer Parameters

parameters/output results		AuNST-800	AuNST-1000	AuNR-800	AuNR-1000	AuNS-520
Au surface density (μg/cm^2)		14−27	18	10−33	12	11
CW laser	energy (J)	25				
	exposure time (s)	40−50	300	20−100	200	300
	optoporation efficacy[a] (%)	90 ± 7	0	88 ± 10	79 ± 19	0
	cell viability[b] (%)	86 ± 12	83 ± 16	68 ± 12	70 ± 18	99 ± 5
pulse laser	pulse energy (mkJ)	1.6	2.7	1.4	1.4	5.7
	pulse frequency (kHz)	10	10	10	10	10
	scanning speed (m/s)	0.02	0.02	0.02	0.02	0.02
	optoporation efficacy[a] (%)	93 ± 6	86 ± 11	78 ± 19	89 ± 9	0
	cell viability[b] (%)	88 ± 11	82 ± 16	65 ± 11	73 ± 16	94 ± 5

[a]Normalized average number of PI$^+$ optoporated cells. [b]Alamar blue data.

7.3% (mcl-1), while those of pro-apoptotic genes increased with 15.4% (caspase 3), 13% (caspase 8), 15% (caspase 9), and 17.3% (bax) comparatively with the expression level of these genes in the control. The expression level of the LAPTM4B gene was overexpressed in sample cells comparatively with control with 45.4%. LAPTM4B gene is known to be a dynamic cancer-associated biomarker that is involved in cell cycle progression, differentiation, DNA damage repair, angiogenesis, and other biological processes.[39] Thus, we conclude that the irradiation with CW and pulsed laser at the defined regimes activate cell self-repair mechanisms and not initiate cell autophagy, apoptosis, or oxidative stress.

Additionally, we demonstrated the excellent ability of the AuNP layers for multiple usages as optoporation platforms. The optoporation performance was maintained at high level as well as cell viability by repeating several times the cycles of HeLa cells cultivation, irradiation, and removal by the trypsinization (data not shown). To summarize, we developed a simple, robust, and scalable technology for AuNP assembling with desired properties and high biocompatibility which can be further commercialized for various applications.

3.2.5. Impact of AuNPs Geometry and PR Wavelength on the Optoporation Performance. Let us consider to one of the crucial questions concerning the understanding of underlying mechanisms behind our optoporation system. Specifically, in this subsection we investigated the impact of AuNPs geometry and PR wavelength on the optoporation performance. For this purpose, we performed a set of HeLa cells optoporation grown AuNST-800 and AuNR-1000 as platforms for CW and pulse laser for PI molecules delivery. AuNS layers with off-resonance particles served as a negative control. The optoporation procedure was carried out following the steps described in section 2.2. The PI delivery efficacy was quantified by processing fluorescent images as described in section S3 (Supporting Information), and the cell viability was checked by the Alamar blue assay as described in section S4 (Supporting Information). Considering the total difference between the used CW and pulsed laser on the optoporation performance, it is worth discussing them separately.

The irradiation regimes for optoporation of HeLa cells with CW laser were optimized in our previous work[24] and set herein as defaults: the laser energy 25 J, the intensity 1 W/cm^2, and the beam defocused to the full irradiated area (the area of the corresponding well). Irradiation time varied from 40−50 s to 200−300 s depending upon the AuNP geometry and corresponding Au content. According to the estimated optoporation efficacy (90 ± 7%) and cell viability (86 ± 12%), we revealed that AuNST-800 layers with 14−27 μg/cm^2 Au content are the most perspective among all others tested. In comparison, the optoporation efficacies for AuNR-800 layers with Au content of 10−33 μg/cm^2 (88 ± 10%) and for AuNST-800 layers were comparable; however, the cell viability was significantly lower (68 ± 12%). The representative images and the viability data are given in Figure S5A,C (Supporting Information). To achieve a sufficient optoporation efficacy (79 ± 19%) for AuNR-1000 layers with PR located distantly from the CW laser wavelength (Figure S1, Supporting Information), we increased significantly the exposure time up to 200 s, so that it affected negatively on cell viability (70 ± 18%). Finally, the AuNST-1000 and AuNS-520 layers, with negligible extinction at 808 nm, were almost unsuitable for optoporation with the CW laser. We observed no optoporated cells after irradiation even with prolonged irradiation up to 300 s (Figure S5A, Supporting Information).

Next, we provided the same set with the pulsed laser. The 2-D scanning mode with precisely focused beam (about 3 μm in diameter) on the well bottom covered with AuNP layers was used for irradiation. The pulse energy was set ranging from 1.4 to 2.7 μJ (varied upon AuNP types and correlating with surface coating). Other parameters were constant and set as follows: pulse duration 200 ns, frequency 10 kHz, and scanning speed 20 mm/s. As a result, the AuNST-800 layers with 14−27 μg/cm^2 Au content again showed the best performance among all other tested plasmonic platforms (Figure S5B,C, Supporting Information). Table 2 summarizes the parameters of AuNP layers and corresponding modes of CW and pulsed lasers irradiation, that were defined as optimal by reaching both maximal values of optoporation efficacy in terms of PI delivery and HeLa cell viability. We speculate that the increased efficiency of cell optoporation on AuNST-800 layers in comparison with other tested AuNP layers can be explained by a broadened plasmon peak of the AuNST-800 spectrum (Figure S1A, Supporting Information). Accordingly, the AuNST-800 particles have strong absorbance at 800 nm as well as at 1064 nm, both matching for two used laser sources.

Then, the low optoporation efficacy estimated for AuNST-1000 and AuNR-1000 can be explained by poorly controlled packing and aggregation of large-sized AuNST-1000 and AuNR-1000 particles (the geometric parameters are given in sections 3.1 and S5, Supporting Information) via CF, resulting in low quality of the layers. Finally, the obtained negative results on the pulse laser for AuNS-520 layers showed that off-resonance particles are almost unsuitable for optoporation. Though, we clarified the plasmonic behavior of the developed optoporation system. We revealed that AuNST-800 layers show the best performance as universal platforms optoporation among all other tested types of AuNPs and can be used both under CW and pulse NIR irradiation.

Let us consider now several illustrative examples that clarify the capabilities of our optoporation system. All subsequent experiments were performed on the AuNST-800 layers under optimized irradiation regimes on HeLa cells with PI fluorescent dye serving as a model nonpenetrating agent for delivery.

3.2.6. Hela Cells Optoporation for Effective PI Delivery Using CW Laser and AuNST-800 Layers. In this section, we describe the correlation between the NPs packing density of the AuNST-800 layers and the efficiency of PI molecules delivery to HeLa cells. The Au content of the layers ranged from 3 to 28 μg/cm^2. The resultant diagram demonstrating the relative number of PI$^+$ cells optoporated on the AuNST-800 layers with gradual Au content is depicted in Figure 3A. The representative fluorescent images are depicted in Figure 3F–H. Phase contrast images captured 30 min post irradiation demonstrate the characteristic morphological changes in irradiated cells (Figure 3B,I) as compared to intact cells (Figure 3D). Nevertheless, no significant effect of laser irradiation was estimated on HeLa cell proliferative activity (according to the data of regular visual monitoring up to 72 h after optoporation), respiratory activity (93 ± 5% according to the Alamar blue assay), and cell monolayer integrity (according to the data of vital FDA staining, Figure S4E, Supporting Information). The detailed explanations of the registered morphophysiological changes in the optoporated HeLa cells will be discussed below in section 3.2.8.

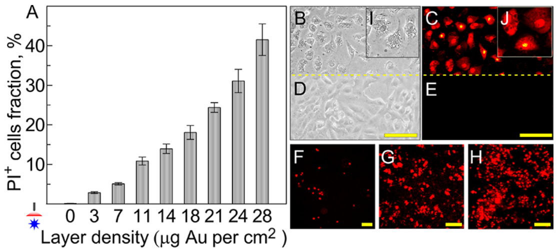

Figure 3. Efficiency of optoporation under CW laser irradiation (A) in terms of relative number of PI-positive cells grown on AuNST-800 layers of different density. Fluorescent images and phase contrast images of control (D and E) and sample cells grown on AuNST-800 layers with Au layer density equal to 7 ± 0.4 (F), 14 ± 1.1 (B, C, G, I, and J), and 28 ± 2.7 μg/cm^2 (H). The scale bars correspond to 50 μm for large-scale images (B–E) and 100 μm for magnified images (F–H).

3.2.7. Precise and Controllable Optoporation of HeLa Cells Using Pulsed Laser and AuNST-800 Layers. The ability to precisely adjust the AuNP layers parameters and corresponding irradiation modes made it possible to achieve the noted high optoporation efficacy. However, the bulk heating of the cell medium during the irradiation evokes potential negative effects both on the cargoes and cells and restricts the usage of CW laser for plasmonic optoporation. On the contrary, the use of a pulsed laser is now considered to be more promising.[20] The main advantages of a pulsed laser are extremely short pulse duration (nano- or femtoseconds) at a relatively low energy, the ability to point-by-point adjustment of individual parameters of the light beam, and the possibility of the 2-D and 3-D scanning irradiation modes to achieve unprecedented high performance. In this regard, herein, we took a pulsed nanosecond 1064 nm laser source with fundamentally different characteristics and mechanisms of action on cell membranes from the previously used 800 nm CW laser. Specifically, we adjusted precisely the optoporation performance by using the pulsed laser source with narrowly focused beam in a 2-D scanning mode across the HeLa cell monolayer grown on the AuNST-800 layers. Figure 4B demonstrates the results of HeLa cells optoporation with a single-cell resolution. The optoporation efficacy (in terms of PI$^+$ cells number) inside the irradiated area was no less than 90–95%. Also, the presented images clearly show the border of the irradiated and nonirradiated areas of the cell monolayer grown on the AuNST-800 layers. It should be noted that the cells morphology significantly differed from the control ones already 15–30 min after irradiation with a pulsed laser. Nevertheless, the viability remained at a high level (93 ± 5% according to the Alamar blue test).

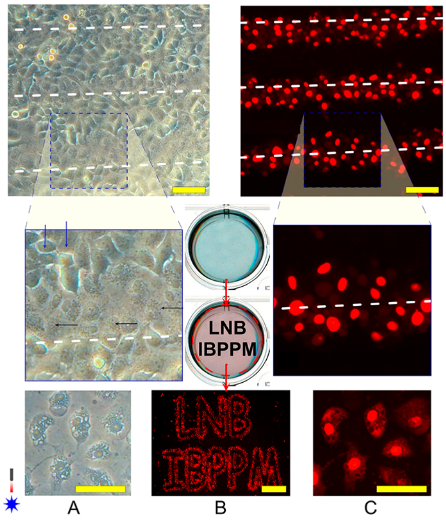

Figure 4. Optoporation of HeLa cells on AuNST-800 layers using a nanosecond 1064 nm pulsed laser. Phase contrast (A) and fluorescent (B and C) images of optoporated cells. Black arrows and white dotted lines show the trajectory of the laser beam. The intact cells are marked with blue arrows. The middle panel (B) shows the scan image of the AuNST-800 layer on the bottom of a 24 well plate, the specified trajectory of irradiation, and the resulting micrograph. Scale bars correspond to 50 μm (top and bottom row, A and C) and 500 μm (bottom row, B).

3.2.8. Underlying Mechanisms of the Plasmon Optoporation and the Peculiarities of the Cells Response under Laser Irradiation. The most interesting and practically unexplored to date are the reversible morphophysiological nondamaging changes of the living cells upon laser irradiation on the AuNP layers. Specifically, we were interested in the nature and duration of the newly formed defects in the lipid bilayer upon cell irradiation which contributes to an increase in permeability for nonpenetrating agents. To this end, we used high-resolution lifetime AFM imaging, bright-field phase contrast microscopy, and fluorescence microscopy.

3.2.8.1. Relationship between Plasmonic Properties of AuNP Layers and the Efficiency of Optoporation. The first question is as follows: whether the increase in membrane permeability upon irradiation of cells on AuNP layers is related

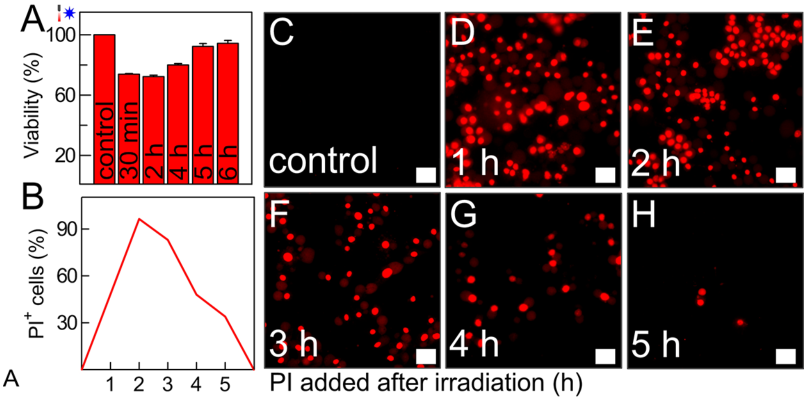

Figure 5. Determination of the self-healing time of the membrane's impermeability upon pulsed laser irradiation. (A) Viability of control and experimental cells, (B) optoporation efficacy and representative fluorescence images of control cells (C) and (D-H) experimental cells with added PI at different times post irradiation. The scale bars correspond to 20 μm.

to the plasmonic properties of AuNPs or just to the thermal effects arising due to conversion of AuNP absorbed laser irradiation to heat. In this regard the effects of CW and pulsed lasers are fundamentally different.[40] We hypothesize that the main mechanism of CW laser optoporation may be associated with local plasmon heating of cell membranes caused by resonant absorption of laser light by AuNST. Recently, several hypotheses[24,41] were proposed to the spontaneous formation of membrane defects due to heating to a phase transition temperature of lipid membranes.[42] It was shown that the increased fluidity of the lipid raft in living cells begins at 42 °C, and a further temperature increase up to 55 °C promotes rapid exchange of low molecular weight (<1 kDa) molecules.[40] To test the thermal hypothesis, we heated the plates with cells grown on the AuNST-800 layers with added PI in a thermal bath up to a temperature of 42 °C of the cell medium. No significant differences were observed in the number of PI$^+$ cells before and after heating (data not shown). Therefore, simple heating of the system cannot be considered as a potential optoporation mechanism. Similarly, negative results were obtained for HeLa cells cultured without AuNP layers (Figures 4 and S6, Supporting Information) and with off-resonance AuNPs upon irradiation with CW or pulsed laser (see the above given results for AuNS-520 layers in section 3.2.5).

3.2.8.2. Duration of Cell Regeneration Processes after IR Laser Irradiation. The next question is addressed to the cells self-repairing to the initial state with retained membrane integrity and impermeability to the large-sized external cargo molecules. It was reported recently that lipid bilayer disruptions, formed by a short-pulsed laser treatment using AuNPs added to the culture medium, completely healed within a few seconds.[43] To study these processes for our optoporation system, we performed an additional experimental set, and the procedure is described in section S7 (Supporting Information). The representative fluorescent images are shown in Figure S7 for the set with PI and in Figures S8 and S9 (Supporting Information) for set with FITC-labeled dextranes. We observed that membrane healing begins already 2 h after optoporation with a CW laser (43 ± 7% PI$^+$ cells; Figure S7B, blue line, Supporting Information), and after 30 h, cell membranes become completely impermeable to PI (Figure S7B, blue line, J, Supporting Information). The cell viability according to the Alamar blue assay was maintained at a high level (Figure S7A, Supporting Information), and the integrity of the membrane was qualitatively confirmed by vital staining of the cell monolayer with FDA dye (Figure S4E, Supporting Information). Considering the irradiation with a pulsed laser, the time required for complete membrane restoration was significantly less than that registered for CW laser irradiation. Already after 30 min, the restoration of membrane integrity began, while the number of PI$^+$ HeLa cells was 95 ± 5%, and 5 h after irradiation, the membranes became completely impermeable to PI (Figure 5B). The cell respiratory activity (according to the Alamar blue assay) measured 30 min post irradiation was slightly decreased to 73 ± 6%, with subsequent restoration to the state of intact cells (93 ± 4%) 5 h post irradiation, (Figure 5A). The similar results were obtained using FITC-labeled dextranes with larger than PI molecule sizes. The self-healing time for membrane integrity was lower than those estimated for PI and reduced when the molecule size increased but still was in the range of 2−4 h (Figures S8 and S9, Supporting Information).

At the moment, we have no reasonable explanation for such a surprisingly long delay required for the completely restoration of the membrane. Meulenberg et al.[44] studied the actin disruption in a cell monolayer upon electric field treatment. The time-elapsed dynamic behavior of the treated cells was quite similar as we registered in the present study, as well as the estimated cell monolayer recovery within the range of 24 h. It was recently demonstrated[45] that complete closure of calcein dye membranes can occur within minutes after irradiation, not within seconds as described in the other study.[43] According to the given explanations,[45] the micrometer pores formed by the cavitation bubble rapidly shrink to exclude the delivery of large molecules, such as DNA plasmids, but remain permeable to small molecules such as PI.

A complete understanding of current mechanisms of the lipid bilayer disruption and cytoskeletal reorganization upon laser irradiation mediated by plasmonic NPs is still lacking. In a recent review authored by Graybill and Davalos,[46] relevant data addressed to this issue was critically discussed. The proposed downstream mechanisms of disruption via interactions between the electromagnetic field and cytoskeletal proteins (or associated proteins) may be related to partial to cytoskeletal disruption through cell swelling, elevated cytosolic calcium levels, ATP depletion, cell signaling, or other pathways. The cellular response to laser irradiation reveals a complex, multifactor process of cytoskeletal response that is undoubtedly influenced by cell type, pulse parameters (pulse

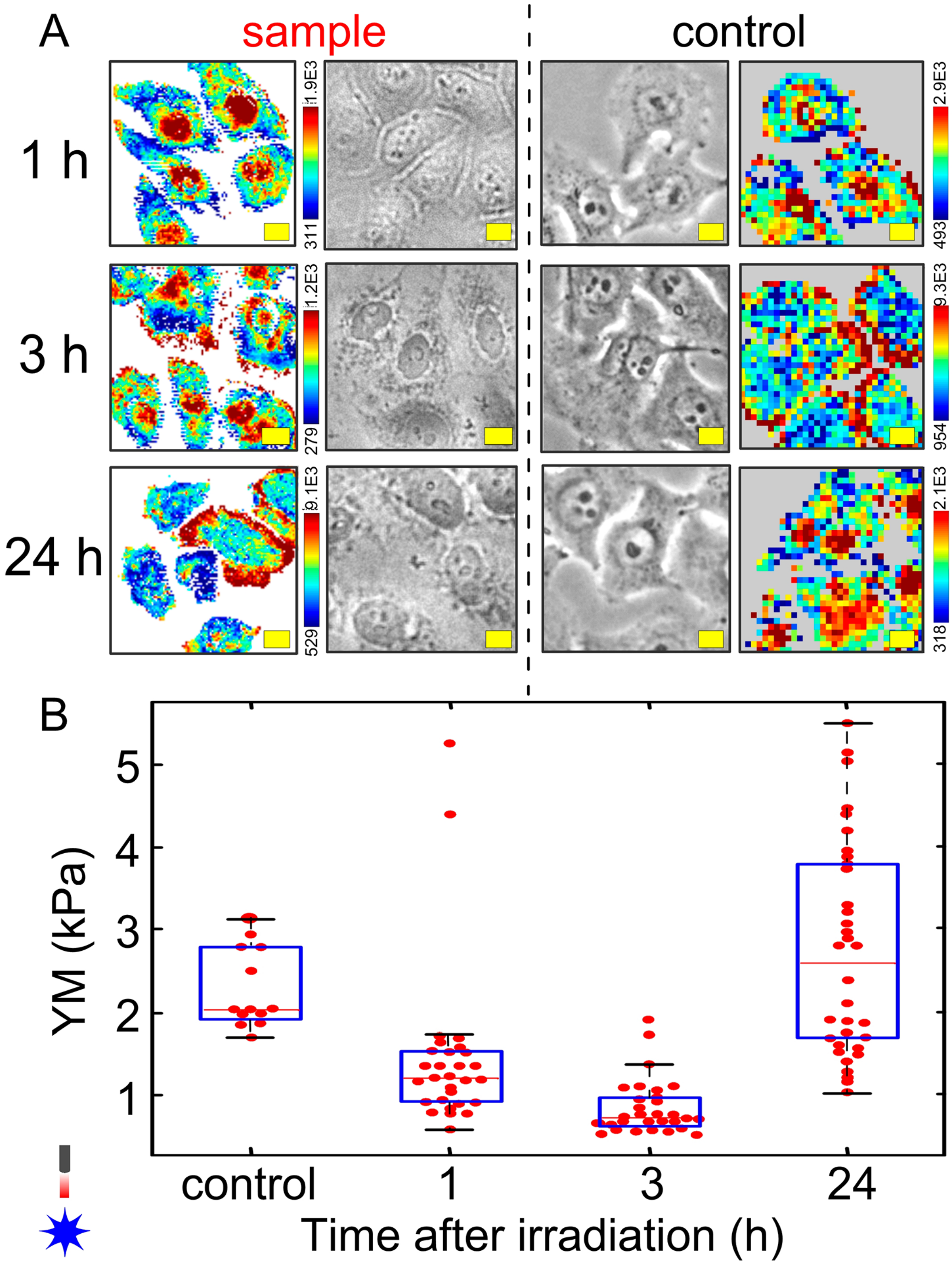

Figure 6. (A) Phase contrast images and AFM maps of mechanical properties of control cells and sample cells, captured 1, 3, and 24 h post irradiation. (B) Distribution of YM in a population of HeLa cells upon pulsed laser irradiation grown on the AuNST-800 layers. Data are presented as mean ± SD for a group of cells, $n = 30$. The scale bars correspond to 10 μm.

length, pulse magnitude, and pulse number), and pulsation media.[46]

Another point that should be addressed is the comparison of the effects of CW laser treatment vs pulsed laser treatment on the cell cytoskeleton and lipid bilayer disruption. The individual regimes of two types of laser irradiation (CW and ns pulsed) were adjusted to provide effective optoporation of HeLa cells grown on AuNP layers without significant loss of their viability. Therefore, it is quite difficult to perform the cell experiments with similar outcomes using different irradiation sources with equivalent modes such as incident intensity, exposure time, single irradiation area, etc. Thus, it is undoubtable that the irradiation upon CW and ns pulse used herein, or other types as referred in numerous recent studies,[46] possess diverse characteristics of cell disruption and recovery.

3.2.8.3. Study of Mechanical Properties of Cells. In addition to the above experiments, we performed a comparative study of the mechanical properties of HeLa cells upon CW and pulse laser irradiation on AuNST-800 layers using the lifetime high-resolution AFM microscopy. A detailed description of sample preparation, scanning modes, and analytical procedures is given in section 2.3. It should be noted that we performed lifetime AFM measurements in precisely optimized conditions using special soft cantilevers with adjusted parameters for living cells. The obtained force curves were corrected using our recently developed algorithm,[31] briefly described in section 2.3. These improvements contributed to minimization of the well-established limitations[47,48] of the AFM technique for soft matter scanning.

Topographic AFM maps were reconstructed from the positions of the points of contact of the curves (z, in μm) and the distribution of YM values. Then the force curves corresponding to individual cells were selected. The resulting summarized data are shown in Figures 6 and S10 (Supporting Information), where the diagrams correspond to the mean YM of individual cells and rectangular areas correspond to medians, 25th and 75th percentiles, respectively.

Irradiation with a CW laser, apparently, caused sharper effects and some signaling cascades leading to an increase in cell stiffness (within 20−24 h after irradiation −10 800 ± 4200 Pa compared to the control −2100 ± 700 Pa, Figure S10, Supporting Information). We assume that the gradual decrease in YM in HeLa cells irradiated with a pulsed laser (from 1600 ± 900 Pa at 1 h post radiation to 1400 ± 500 Pa within next 5 h) may be associated with a weakening of the structure of the actin cytoskeleton. The restoration of the cytoskeleton occurred at the same time as the restoration of the plasma membrane and the general state of cells, as can be seen from parallel experiments on intracellular delivery of PI (Figures 5B and S7B, Supporting Information).

Here, a significant difference in mechanical response was found for cells irradiated with CW and pulsed lasers. Cell mechanical properties might reflect the overall stressed state of a cell. Changes in the cell stiffness, usually a decrease, were observed under adverse actions caused, for example, by incubation with NPs[49,50] or by cold storage.[51] Modifications in cell mechanical properties, as it was shown in a range of previous studies, are related to the changes in the cytoskeleton structure.[52−54] Primarily, the actin cytoskeleton was found to be responsible for cell mechanical properties as measured by AFM. Indeed, cytoskeleton modification was directly shown in optoporated cells by means of the fluorescent microscopy[55] and manifested in a decrease in alignment, or coherency, of actin fibers. Since the actin cytoskeleton (specifically, actin cortex) is linked to the cell membrane, structural changes in the latter, including the membrane resealing will cause actin structure modification as well.[56] Moreover, disturbance in the concentration of intracellular signal molecules and ions leaking through the membrane pores might cause global long-lasting actin rearrangements. Additionally, we estimated the average cell size by processing the phase-contrast images and AFM images of control cells and sample cells at different elapsed times post irradiation (0, 0.5, 1, 2, 3, 20, and 24 h after irradiation). It was maintained in the range of 50−55 μm, which is typical for HeLa cells, thus confirming that the irradiation by CW and pulsed laser with set regimes does not generate drastic changes in cell morphology.

With the above considerations, we might link a decrease in the YM observed in the cells irradiated with the pulsed lasers to the weakening of the actin cytoskeleton structure (Figure 6A). Recovery of the cytoskeleton occurred on the same time scales as the recovery of the plasma membrane and overall cell condition, as seen from the experiments with PI entrance. The irradiation with a CW laser, apparently, caused more drastic effects and some signal cascades leading to an increase in the cell stiffness. These cascades might have a protective role for the cell nucleus. In a previous study,[56] a significant increase in cell stiffness was also observed during progression of the cell death and loss of membrane integrity, and similar effects might be observed here. However, in our case, these effects seem to be mostly recoverable and do not lead to cell death.

4. CONCLUSIONS

The performed investigations were aimed at a comprehensive study of the developed optoporation system on the plasmonic NPs layers, as well as reactions from the cells under the influence of laser irradiation. First, we have thoroughly characterized by optical and microscopic methods the physicochemical parameters of the layers of gold nanostars and nanorods. Second, we showed the possibility of adjusting the optoporation efficacy by controlling the individual parameters of monolayers (packing density and coating uniformity) and the irradiation modes with pulsed and CW IR lasers. Third, we studied the dynamics of changes in the mechanical properties of HeLa cells upon laser irradiation. The high cell viability and unchanged plasmonic and geometric properties of NPs, confirmed at all stages of experiments, make it possible to judge the safety of our developed system. We expect that the our optoporation system can be adjusted for effective transfection of other types of cells after appropriate optimization steps, for example primary or stem cells, that are known as hard-to-transfect cells. Fourth, the developed combined AFM-based approach with fluorescent microscopy and qRT-PCR can be used in similar studies of the morphological and functional state of the cells exposed to the influence of other external conditions. We have demonstrated long-term permeability of cell membranes for delivered fluorescent dyes for at least 2−3 h after optoporation via pulsed laser and more than 20 h upon CW laser optoporation on AuNP layers without affecting the cell viability. We believe that the observed effects of such a long self-healing of cells after optoporation, which do not lead to their death, are interesting not only from a fundamental but also from a practical point of view. Further investigations are needed to reveal the duration of cell membranes permeability for plasmid or RNAi-based vectors.

■ ASSOCIATED CONTENT

Supporting Information

The Supporting Information is available free of charge at https://pubs.acs.org/doi/10.1021/acsanm.1c02734.

List of chemicals; AuNP fabrication protocols; AuNP colloids and layers characterization by UV−vis spectroscopy, DLS, TEM, AFM imaging, surface packing density calculations, photo- and chemical stability, and biocompatibility tests; qRT-PCR analysis description; optoporation efficacy quantification and cell viability assays; the impact of AuNPs geometry and PR wavelength on the optoporation outcome; the cell recovery investigations; AFM study of mechanical properties of HeLa cells (PDF)

■ AUTHOR INFORMATION

Corresponding Author

Timofey E. Pylaev − *Institute of Biochemistry and Physiology of Plants and Microorganisms, Russian Academy of Sciences, Saratov 410049, Russia; Saratov State Medical University n.a. V.I. Razumovsky, Saratov 410012, Russia; Federal Center of Agriculture Research of the South-East Region,* *Saratov 410010, Russia;* orcid.org/0000-0002-2701-3333; Email: pylaev_t@ibppm.ru

Authors

Yuri Efremov – *Institute for Regenerative Medicine, Sechenov University, Moscow 119991, Russia; World-Class Research Center "Digital biodesign and personalized healthcare", Sechenov First Moscow State Medical University, Moscow 119991, Russia*

Elena S. Avdeeva – *Institute of Biochemistry and Physiology of Plants and Microorganisms, Russian Academy of Sciences, Saratov 410049, Russia*

Artem A. Antoshin – *Institute for Regenerative Medicine, Sechenov University, Moscow 119991, Russia;* orcid.org/0000-0003-0575-0321

Anastasiia I. Shpichka – *Institute for Regenerative Medicine, Sechenov University, Moscow 119991, Russia; Chemistry Department, Lomonosov Moscow State University, Moscow 119991, Russia; World-Class Research Center "Digital biodesign and personalized healthcare", Sechenov First Moscow State Medical University, Moscow 119991, Russia*

Tatiana M. Khlebnikova – *Institute for Regenerative Medicine, Sechenov University, Moscow 119991, Russia; Institute for Urology and Reproductive Health, Sechenov University, Moscow 119991, Russia*

Peter Timashev – *Institute for Regenerative Medicine, Sechenov University, Moscow 119991, Russia; Chemistry Department, Lomonosov Moscow State University, Moscow 119991, Russia; World-Class Research Center "Digital biodesign and personalized healthcare", Sechenov First Moscow State Medical University, Moscow 119991, Russia*

Nikolai G. Khlebtsov – *Institute of Biochemistry and Physiology of Plants and Microorganisms, Russian Academy of Sciences, Saratov 410049, Russia; Saratov State University, Saratov 410012, Russia;* orcid.org/0000-0002-2055-7784

Complete contact information is available at:
https://pubs.acs.org/10.1021/acsanm.1c02734

Notes

The authors declare no competing financial interest.

ACKNOWLEDGMENTS

The work by P.T.E. was supported by the Saratov State Medical University according to the research project No. SSMU-2021-001 (cells optoporation experiments). The part of the work on nanoparticle layers preparation was funded by Russian Science Foundation Project No 18-14-00016-П. AFM imaging and data analysis were supported by the Russian Science Foundation (21-15-00339). The study was performed using the unique scientific facility Transgenebank.

ABBREVIATIONS

AFM, atomic force microscopy; AuNP, gold nanoparticles; PI, propidium iodide; YM, Young's modulus; CW, continuous-wave; CF, centrifuge; PR, plasmon resonance; AuNST, gold nanostars; AuNR, gold nanorods; AuNS, gold nanospheres; PEG, polyethylene glycol; TEM, transmission electron microscopy; SEM, scanning electron microscopy; PVP, polyvinylpyridine; DLS, dynamic light scattering; CTAB, cetyltrimethylammonium bromide; FDA, fluorescein diacetate

REFERENCES

(1) Duckert, B.; Vinkx, S.; Braeken, D.; Fauvart, M. Single-cell transfection technologies for cell therapies and gene editing. *J. Controlled Release* **2021**, *330*, 963–975.

(2) Váňová, J.; Hejtmánková, A.; Kalbáčová, M. H.; Španielová, H. The Utilization of cell-penetrating peptides in the intracellular delivery of viral nanoparticles. *Materials* **2019**, *12* (17), 2671.

(3) Hardee, C. L.; Arévalo-Soliz, L. M.; Hornstein, B. D.; Zechiedrich, L. Advances in non-viral DNA vectors for gene therapy gene editing. *Genes* **2017**, *8* (2), 65.

(4) Park, S. E.; Sajid, M. I.; Parang, K.; Tiwari, R. K. Cyclic cell-penetrating peptides as efficient intracellular drug delivery tools. *Mol. Pharmaceutics* **2019**, *16* (9), 3727–3743.

(5) Hasan, M. N.; Nafiujjaman, M.; Lee, Y.-K. 2D nanomaterials for gene delivery. *Biomedical Applications of Graphene and 2D Nanomaterials*; Nurunnabi, Md., McCarthy, J., Eds.; Elsevier, 2019; pp 866.

(6) Chen, G.; Roy, I.; Yang, C.; Prasad, P. N. Nanochemistry and nanomedicine for nanoparticle-based diagnostics and therapy. *Chem. Rev.* **2016**, *116*, 2826–2885.

(7) Xu, H.; Li, Z.; Si, J. Nanocarriers in gene therapy: A review. *J. Biomed. Nanotechnol.* **2014**, *10*, 3483–3507.

(8) Guo, K.; Zhao, X.; Dai, X.; Zhao, N.; Xu, F.-J. Organic/inorganic nanohybrids as multifunctional gene delivery systems. *J. Gene Med.* **2019**, *21* (5), e3084.

(9) Niu, Y.; Popat, A.; Yu, M.; Karmakar, S.; Gu, W.; Yu, C. Recent advances in the rational design of silica-based nanoparticles for gene therapy. *Ther. Delivery* **2012**, *3*, 1217–1237.

(10) Mokhtarzadeh, A.; Vahidnezhad, H.; Youssefian, L.; Mosafer, J.; Baradaran, B.; Uitto, J. Applications of spherical nucleic acid nanoparticles as delivery systems. *Trends Mol. Med.* **2019**, *25*, 1066–1079.

(11) Hornos Carneiro, M. F.; Barbosa, F. Gold nanoparticles: A critical review of therapeutic applications and toxicological aspects. *J. Toxicol. Environ. Health, Part B* **2016**, *19* (3–4), 129–148.

(12) Dykman, L. A.; Khlebtsov, N. G. Multifunctional gold-based nanocomposites for theranostics. *Biomaterials* **2016**, *108*, 13–34.

(13) Baghban Taraghdari, Z.; Imani, R.; Mohabatpour, F. A review on bioengineering approaches to insulin delivery: a pharmaceutical and engineering perspective. *Macromol. Biosci.* **2019**, *19* (4), 1800458.

(14) Dykman, L. A.; Khlebtsov, N. G. Gold nanoparticles in chemo-, immuno-, and combined therapy: review [Invited]. *Biomed. Opt. Express* **2019**, *10* (7), 3152.

(15) Dykman, L. A.; Khlebtsov, N. G. Methods for chemical synthesis of colloidal gold. *Russ. Chem. Rev.* **2019**, *88* (3), 229–247.

(16) Venditti, I. Morphologies and functionalities of polymeric nanocarriers as chemical tools for drug delivery: A review. *J. King Saud Univ., Sci.* **2019**, *31* (3), 398–411.

(17) Lachaine, R.; Boulais, É.; Meunier, M. From thermo- to plasma-mediated ultrafast laser-induced plasmonic nanobubbles. *ACS Photonics* **2014**, *1* (4), 331–336.

(18) Du, X.; Wang, J.; Zhou, Q.; Zhang, L.; Wang, S.; Zhang, Z.; Yao, C. Advanced physical techniques for gene delivery based on membrane perforation. *Drug Delivery* **2018**, *25*, 1516–1525.

(19) Courvoisier, S.; Saklayen, N.; Huber, M.; Chen, J.; Diebold, E. D.; Bonacina, L.; Wolf, J.-P.; Mazur, E. Plasmonic tipless pyramid arrays for cell poration. *Nano Lett.* **2015**, *15*, 4461–4466.

(20) Saklayen, N.; Huber, M.; Madrid, M.; Nuzzo, V.; Vulis, D. I.; Shen, W.; Nelson, J.; McClelland, A. A.; Heisterkamp, A.; Mazur, E. Orcid intracellular delivery using nanosecond-laser excitation of large-area plasmonic substrates. *ACS Nano* **2017**, *11*, 3671–3680.

(21) Man, T.; Zhu, X.; Chow, Y. T.; Dawson, E. R.; Wen, X.; Patananan, A. N.; Liu, T. L.; Zhao, C.; Wu, C.; Hong, J. S.; Chung, P.-S.; Clemens, D. L.; Lee, B.-Y.; Weiss, P. S.; Teitell, M. A.; Chiou, P.-Y. Intracellular photothermal delivery for suspension cells using sharp nanoscale tips in microwells. *ACS Nano* **2019**, *13*, 10835–10844.

(22) Lyu, Z.; Zhou, F.; Liu, Q.; Xue, H.; Yu, Q.; Chen, H. A universal platform for macromolecular deliveryinto cells using gold nanoparticle layers via the photoporation effect. *Adv. Funct. Mater.* **2016**, *26* (32), 5787–5795.

(23) Pylaev, T.; Avdeeva, E.; Khlebtsov, B.; Zakharevich, A.; Khlebtsov, N. A novel centrifuge-based approach for tunable 2D layering of plasmonic nanoparticles. *Proc. SPIE* **2018**, *11067*, 110671I.

(24) Pylaev, T.; Vanzha, E.; Avdeeva, E.; Khlebtsov, B.; Khlebtsov, N. A novel cell transfection platform based on laser optoporation mediated by Au nanostar layers. *J. Biophotonics.* **2019**, *12*, e201800166.

(25) Vanzha, E.; Pylaev, T.; Prilepskii, A.; Golubev, A.; Khlebtsov, B.; Bogatyrev, V.; Khlebtsov, N. Cell culture surfaces with immobilized gold nanostars: a new approach for laser-induced plasmonic cell optoporation. *Proc. SPIE* **2016**, 10336.

(26) Bisker, G.; Yelin, D. Noble-metal nanoparticles and short pulses for nanomanipulations: theoretical analysis. *J. Opt. Soc. Am. B* **2012**, *29*, 1383−1393.

(27) Stewart, M. P.; Langer, R.; Jensen, K. F. Intracellular delivery by membrane disruption: mechanisms, strategies, and concepts. *Chem. Rev.* **2018**, *118*, 7409−7531.

(28) Schomaker, M.; Killian, D.; Willenbrock, S.; Heinemann, D.; Kalies, S.; Ngezahayo, A.; Nolte, I.; Ripken, T.; Junghanß, C.; Meyer, H.; Escobar, H. M.; Heisterkamp, A. Biophysical effects in off resonant gold nanoparticle mediated (GNOME) laser transfection of cell lines, primary and stem cells using fs laser pulses. *J. Biophotonics.* **2015**, *8*, 646−658.

(29) Schillers, H.; Rianna, C.; Schäpe, J.; Luque, T.; Doschke, H.; Wälte, M.; Uriarte, J. J.; Campillo, N.; Michanetzis, G. P. A.; Bobrowska, J.; Dumitru, A.; Herruzo, E. T.; Bovio, S.; Parot, P.; Galluzzi, M.; Podestà, A.; Puricelli, L.; Scheuring, S.; Missirlis, Y.; Garcia, R.; Odorico, M.; Teulon, J.-M.; Lafont, F.; Lekka, M.; Rico, F.; Rigato, A.; Pellequer, J.-L.; Oberleithner, H.; Navajas, D.; Radmacher, M. Standardized nanomechanical atomic force microscopy procedure (SNAP) for measuring soft and biological samples. *Sci. Rep.* **2017**, *7*, 5117.

(30) Efremov, Y. M.; Wang, W.-H.; Hardy, S. D.; Geahlen, R. L.; Raman, A. Measuring nanoscale viscoelastic parameters of cells directly from AFM force-displacement curves. *Sci. Rep.* **2017**, *7*, 1541.

(31) Efremov, Y. M.; Shpichka, A. I.; Kotova, S.; Timashev, P. S. Viscoelastic mapping of cells based on fast force volume and peakforce tapping. *Soft Matter* **2019**, *15*, 5455.

(32) Garcia, P. D.; Garcia, R. Determination of the elastic moduli of a single cell cultured on a rigid support by force microscopy. *Biophys. J.* **2018**, *114*, 2923−2932.

(33) Maksimova, I. L.; Akchurin, G. G.; Terentyuk, G. S.; Khlebtsov, B. N.; Akchurin, G. G., Jr.; Ermolaev, I. A.; Skaptsov, A. A.; Revzina, E. M.; Tuchin, V. V.; Khlebtsov, N. G. Laser photothermolysis of biological tissues by using plasmon-resonance particles. *Quantum Electron.* **2008**, *38*, 536−542.

(34) Khlebtsov, N. G.; Zarkov, S. V.; Khanadeev, V. A.; Avetisyan, Y. A. A novel concept of two-component dielectric function for gold nanostars: theoretical modelling and experimental verification. *Nanoscale* **2020**, *12*, 19963−19981.

(35) Khlebtsov, B. N.; Khanadeev, V. A.; Panfilova, E. V.; Khlebtsov, N. G. Improved size-tunable synthesis and SERS properties of Au nanostars. *J. Nanopart. Res.* **2014**, *16*, 2623.

(36) Khlebtsov, B.; Khanadeev, V.; Pylaev, T.; Khlebtsov, N. A. New T-Matrix solvable model for nanorods: TEM-based ensemble simulations supported by experiments. *J. Phys. Chem. C* **2011**, *115*, 6317−6323.

(37) Ray, P. Ch.; Yu, H.; Fu, P. P. Toxicity and environmental risks of nanomaterials: challenges and future needs. *J. Environ. Sci. Heal.* **2009**, *27*, 1−35.

(38) Haq, S.; Tesema, T. E.; Patra, B.; Gomez, E.; Habteyes, T. G. Tuning plasmonic coupling from capacitive to conductive regimes via atomic control of dielectric spacing. *ACS Photonics* **2020**, *7* (3), 622−629.

(39) Meng, F.; Chen, X.; Song, H.; Lou, G. LAPTM4B down regulation inhibits the proliferation, invasion and angiogenesis of Hela cells *in vitro*. *Cell. Physiol. Biochem.* **2015**, *37*, 890−900.

(40) Gu, L.; Koymen, A. R.; Mohanty, S. K. Crystalline magnetic carbon nanoparticle assisted photothermal delivery into cells using CW near-infrared laser beam. *Sci. Rep.* **2015**, *4*, 5106.

(41) El-Andaloussi, S.; Järver, P.; Johansson, H. J.; Langel, Ü. Cargo-dependent cytotoxicity and delivery efficacy of cell-penetrating peptides: a comparative study. *Biochem. J.* **2007**, *407*, 285−292.

(42) Gilbert, R. Inactivation and activity of cholesterol-dependent cytolysins: What structural studies tell us. *Cell. Mol. Life Sci.* **2002**, *59*, 832−844.

(43) Kalies, S.; Heinemann, D.; Schomaker, M.; Gentemann, L.; Meyer, H.; Ripken, T. Immobilization of gold nanoparticles on cell culture surfaces for safe and enhanced gold nanoparticle-mediated laser transfection. *J. Biomed. Opt.* **2014**, *19*, 070505.

(44) Meulenberg, C. J. W.; Todorovic, V.; Cemazar, M. Differential cellular effects of electroporation and electrochemotherapy in monolayers of human microvascular endothelial cells. *PLoS One* **2012**, *7*, e52713.

(45) Wu, Y.-C.; Wu, T.-H.; Clemens, D. L.; Lee, B.-Y.; Wen, X.; Horwitz, M. A.; Teitell, M. A.; Chiou, P.-Y. Massively parallel delivery of large cargo into mammalian cells with light pulses. *Nat. Methods* **2015**, *12*, 439−444.

(46) Graybill, P. M.; Davalos, R. V. Cytoskeletal disruption after electroporation and its significance to pulsed electric field therapies. *Cancers* **2020**, *12*, 1132.

(47) Dimitriadis, E. K.; Horkay, F.; Maresca, J.; Kachar, B.; Chadwick, R. S. Determination of elastic moduli of thin layers of soft material using the atomic force microscope. *Biophys. J.* **2002**, *82*, 2798−2810.

(48) Butt, H.-J.; Cappella, B.; Kappl, M. Force measurements with the atomic force microscope: Technique, interpretation and applications. *Surf. Sci. Rep.* **2005**, *59*, 1−152.

(49) Pi, J.; Yang, F.; Jin, H.; Huang, X.; Liu, R.; Yang, P.; Cai, J. Selenium nanoparticles induced membrane bio-mechanical property changes in MCF-7 cells by disturbing membrane molecules and F-Actin. *Bioorg. Med. Chem. Lett.* **2013**, *23*, 6296−6303.

(50) Pastrana, H. F.; Cartagena-Rivera, A. X.; Raman, A.; Ávila, A. Evaluation of THE Elastic Young's modulus and cytotoxicity variations in fibroblasts exposed to carbon-based nanomaterials. *J. Nanobiotechnol.* **2019**, *17*, 32.

(51) Nikolaev, N. I.; Müller, T.; Williams, D. J.; Liu, Y. Changes in the Stiffness of human mesenchymal stem cells with the progress of cell death as measured by atomic force microscopy. *J. Appl. Biomech.* **2014**, *47*, 625−630.

(52) Efremov, Y. M.; Velay-Lizancos, M.; Weaver, C. J.; Athamneh, A. I.; Zavattieri, P. D.; Suter, D. M.; Raman, A. Anisotropy vs isotropy in living cell indentation with AFM. *Sci. Rep.* **2019**, *9*, 5757.

(53) Rotsch, C.; Radmacher, M. Drug-Induced Changes of cytoskeletal structure and mechanics in fibroblasts: an atomic force microscopy study. *Biophys. J.* **2000**, *78*, 520−535.

(54) Kwon, S.; Kim, K. S. Qualitative analysis of contribution of intracellular skeletal changes to cellular elasticity. *Cell. Mol. Life Sci.* **2020**, *77*, 1345−1355.

(55) Saklayen, N.; Kalies, S.; Madrid, M.; Nuzzo, V.; Huber, M.; Shen, W.; Sinanan-singh, J.; Heinemann, D.; Heisterkamp, A.; Mazur, E. Analysis of poration-induced changes in cells from laser-activated plasmonic substrates. *Biomed. Opt. Express* **2017**, *8*, 4756−4771.

(56) McNeil, P. L.; Terasaki, M. Coping with the Inevitable: how cells repair a torn surface membrane. *Nat. Cell Biol.* **2001**, *3*, E124−E129.